Strength and Microstructure of Laser Fusion Welded Ti-SS Dissimilar Material Pair

Gen Satoh, Y. Lawrence Yao
Department of Mechanical Engineering
Columbia University
New York, NY USA

Caian Qiu
Champaign Simulation Center
Caterpillar
Champaign, IL, USA

ABSTRACT

The ability to efficiently create robust and reliable dissimilar metal joints has the potential to enable new functionalities and reduce the manufacturing costs of medical devices. The need for dissimilar material welds in the medical device industry is driven by the unique properties exhibited by biocompatible materials such as stainless steel and titanium, as well as shape memory materials such as NiTi. Many material pairs, however, suffer from significant intermetallic phase formation during welding which greatly reduces their strength. This study investigates the microstructures and strength of the laser fusion welded titanium-stainless steel dissimilar material pair as a simplified model of the NiTi-stainless steel pair. Compositional and structural analysis of the weld pool is performed and fracture morphologies are analyzed in different regions of the weld joint. The role of weld pool geometry, heat flow, and quench rate on the resultant phases, microstructures, and strength of the welds is discussed.

KEYWORDS

Laser Welding, Dissimilar Material Welding, Stainless Steel, Titanium, Intermetallic

INTRODUCTION

Joining of dissimilar materials is performed in order to take advantage of specific attributes of each material to enhance the performance of a product or introduce new functionalities. The need to join two different materials typically arises when one possesses an attribute that is required for functionality of the device but also has some inherent disadvantages such as increased cost or weight and thus cannot be used extensively. Some attributes of interest are corrosion resistance and biocompatibility, thermal and electrical properties, as well as mechanical properties such as Young's modulus and hardness. In the case where one material is a smart material such as a shape memory alloy, specific attributes such as superelasticity or the shape memory effect may also be exploited.

A number of dissimilar material joints have been successfully formed using various methods from fusion welding to diffusion bonding including metal-metal, metal-ceramic, and metal-polymer joints [1] . Materials with good compatibility such as Cu and Ni can be joined using fusion processes while pairs that form phases with undesirable properties upon mixing are typically joined in the solid state [2] or with the aid of a non-reactive interlayer [3][4]. Dissimilar metal welding (DMW) of the bio-compatible materials stainless steel (SS) and the shape memory alloy Nickel-Titanium (NiTi) is of particular interest within the bio-medical industry due to the exceptional mechanical properties of NiTi and the low cost of stainless steel 316. This particular material pair, however, suffers from significant intermetallic formation after mixing which results in brittle joints which are unable to withstand handling and use [5]. A number of intermetallic phases exist even in the simplified binary Fe-Ti system as shown in Fig. 1 [6]. The addition of alloying elements such as Cr and Ni found in SS and NiTi introduces further complexities in microstructure and phase formation. The dissimilar material pair between stainless steel and titanium alleviates some of these complexities by reducing the nickel composition from roughly 50 at% in the NiTi to only ~10 at% in the SS while still enabling the formation of Ti-Fe-based intermetallics.

Traditional joining methods such as arc welding when applied to dissimilar material pairs have been found to introduce excessive amounts of heat resulting in the formation of large volumes of intermetallics [7]. Some success has been found through the use of laser welding due to its precise, localized heat input capabilities which allows for small heat affected zones, however, the joints still suffer

from brittle intermetallic formation [8]. Li, et al. have used laser brazing to join NiTi and SS through the use of silver-based filler materials, however, the addition of filler materials during welding adds significant complexity to the process and the filler material is not able to achieve corrosion resistances comparable to the base materials [9]. Diffusion bonding, where two materials are pushed together at high pressure and temperature in the solid state for extended periods of time to form a bond, has shown some success but requires strict tolerances on surface flatness, significant time, and the ability to impart large stresses on the materials [10]. These requirements are increasingly difficult to achieve as devices are created at small length scales as found within bio-medical devices. Ultrasonic welding, which uses pressure and high-frequency vibrations to create solid state joints, has been shown to produce strong welds in a number of dissimilar metal pairs but is limited to lap joints and can be difficult to perform on thick sections and on strong and hard materials such as Ti [11]. A robust fusion welding process for the NiTi-SS pair would allow for reliable and efficient formation of strong joints for bio-medical applications. The development of such a process requires comprehensive understanding of the microstructures and failure mechanisms observed in this material pair in the fusion welding regime.

In this study the use of pulsed laser welding to join titanium to SS 316 is investigated through the use of energy-dispersive x-ray spectroscopy (EDX) and electron backscatter diffraction (EBSD) for compositional and microstructural analysis. Fracture surface analysis is performed through scanning electron microscopy and EDX. Computational thermodynamics techniques are used to model phase evolution during solidification of multi-component systems.

BACKGROUND

Equilibrium Phases

The SS – Ti pair, while attractive for many applications, is not widely used due to the existence of multiple brittle intermetallics within the Fe-Ti phase diagram. Stainless steel, with a composition primarily consisting of Fe, Cr, and Ni, will form many of the same phases when combined with Ti as observed in the Fe-Ti material pair and thus suffers from many of the same issues with regards to mechanical strength and ductility. Figure 1 is a binary phase diagram containing the two main components expected in a SS-Ti dissimilar material weld, Fe and Ti [6]. While ternary Fe-Ti-Cr and Fe-Ti-Ni phase diagrams are available, the phases formed differ very little from the binary diagram at the Cr and Ni compositions found in SS. Phases omitted in the binary diagram are $NiTi_2$ and $TiCr_2$, which are expected to form in small amounts in a SS-Ti mixture. On the binary phase diagram a few phases are formed, namely α-Ti, β-Ti, FeTi, λ, and α-Fe, in order of increasing Fe content.

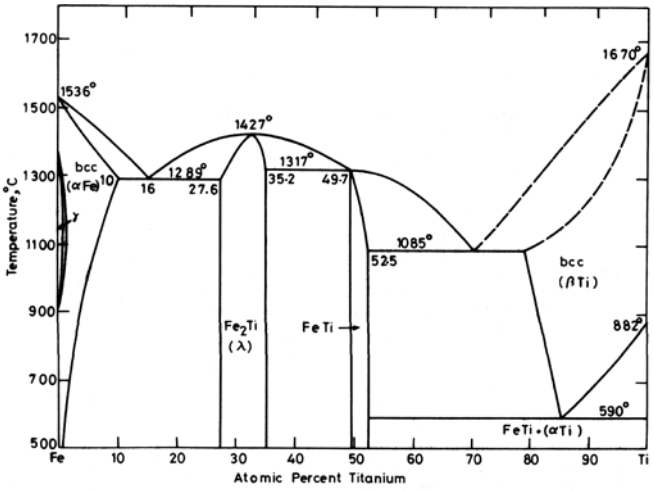

Figure 1. Fe-Ti binary phase diagram showing existence of at least two intermetallic phases in the stainless steel - Nickel Titanium material pair [6] .

In this case λ represents $TiFe_2$ which has a C14 hexagonal Laves intermetallic structure. In the ternary Fe-Ti-Cr phase diagram, λ represents a solid solution of $TiFe_2$ and $TiCr_2$. The λ-Laves phase is close-packed and has a homogeneity range between 64.8 and 72.4 at% Fe. β-Ti has a base-centered cubic (BCC) structure which at equilibrium will transform to α-Ti and TiFe through a eutectoid reaction. The intermetallic FeTi also has a BCC structure and only exists between 47.5 and 50.2 at% Fe. α-Fe also has a BCC structure.

Eutectic Solidification

As can be seen in Fig. 1, a eutectic reaction occurs on the Ti-rich side with the formation of β-Ti and TiFe from liquid. At equilibrium the formation of these two phases is typically in a lamellar structure with alternating β-Ti and TiFe plates. The microstructure is divided into colonies within which each set of plates has the same crystal orientation and a specific orientation relationship that aims to minimize the interfacial energy between the two phases. At higher cooling rates directionality is observed in the growth of the plates resulting in an oriented microstructure with the plates aligned in the direction of heat flow.

It has been shown by Yu, et al. that during solidification of near-eutectic compositions in the Ti-Fe pair that a supersaturated β-Ti(Fe) solid solution will form first followed by the FeTi intermetallic phase [11]. Dendrites in this material pair are typically in the form of TiFe dendrites within a supersaturated β-Ti(Fe) matrix. As with other eutectic structures solidified under a thermal gradient, the dendrites will form preferentially in the direction of heat flow. While it has been shown by Louzguine-Luzgin, et al.

that the interfaces between coarse TiFe dendrites and the matrix cause crack propagation to be arrested [12], the formation of a directional dendritic structure introduces a great deal of anisotropy to the mechanical properties of the material which typically show significantly more robust mechanical properties along the dendrite growth direction and limited strength in the transverse direction.

While strict observation of the equilibrium phase diagram (Fig. 1) suggests that α-Ti, the HCP structured Ti phase, should form below 595°C, it has been shown that a number of factors can stabilize the β-phase. One of the strongest effects comes from alloying. A number of elements such as Mo, V, W, Nb, Ta, Fe, and Cr have been shown to be β-stabilizers meaning that their existence lowers the α/β transus. Still other elements such as Al and O are α-stabilizers and have the opposite effect. The overall effect of these elements in captured by calculating the %Mo-equivalent composition which is written as [13]

$$\begin{aligned} \%Mo\ Equivalent &= 1.0(\%Mo) + 0.67(\%V) \\ &+0.44(\%(W) + 0.28(\%Nb) + 0.22(\%Ta) \\ &+2.9(\%Fe)+1.6(\%Cr)\text{-}1.0(\%Al) \end{aligned} \quad (1)$$

It is suggested that for %Mo-equivalent values exceeding 10%, a β-alloy will form. In the Ti-Fe pair, only a small amount of mixing is required to exceed the 10% Mo-equivalent threshold. In addition to compositional changes that stabilize the β-phase, extended solubility of Fe in β-Ti has also been observed at high cooling rates [14]. This allows for the formation of single-phase β-Ti(Fe) at compositions outside the equilibrium homogeneity range.

NUMERICAL MODELING

While binary and tertiary phase diagrams are useful for understanding the effects of the two or three main alloy components on the phases formed during welding, they are unable to take into account any more than three components. In order to account for the effects of larger numbers of components, computational thermodynamics techniques are often used. The basis for phase prediction using computational thermodynamics is the calculation of the free energies of different phases in a material as a function of temperature, *T*, pressure, *P*, and composition, *X*. For a mechanical mixture between two pure components the free energy can be written as [15]

$$G^M = X_A H_A + X_B H_B - T(X_A S_A + X_B S_B) \quad (2)$$

Where X_i are the mole fractions, H_i are the enthalpies, and S_i are the entropies of the pure components *A* and *B*. If, however, a solution is created, the free energy is written as

$$G^S = X_A \bar{H}_A + X_B \bar{H}_B - T(X_A \bar{S}_A + X_B \bar{S}_B) - T\Delta S_M \quad (3)$$

Where barred quantities indicate values when in solution and ΔS_M is the entropy of mixing which accounts for the configurational entropy of the solution. For dilute solutions the configurational entropy can be written as

$$\Delta S_M = -R(X_A \ln X_A + X_B \ln X_B) \quad (4)$$

For non-ideal solutions where properties in the solution and in pure form are different, the free energy is written as

$$\begin{aligned} G^S &= G^M + X_A(\bar{H}_A - H_A) \\ &+X_B(\bar{H}_B - H_B) \\ &-T[X_A(\bar{S}_A - S_A) + X_B(\bar{S}_B - S_B)] \\ &+RT(X_A \ln X_A + X_B \ln X_B) \\ &= G^M + \Delta H^{xs} - T\Delta S^{xs} - T\Delta S_M \end{aligned} \quad (5)$$

Where *xs* quantities are the difference of the value relative to an ideal solution.

Equation 5 thus represents the free energy of a specific phase as a function of temperature and composition with pressure typically held constant. Once these relationships are known for each phase in the material, an equilibrium phase diagram can be created by plotting the phase which has the lowest free energy at each composition and temperature. This is the basis of the CALPHAD (CALculation of PHAse Diagrams) method.

In order to extend these equations past binary combinations to higher order systems, extra terms are added for each new component and higher-order free energy "surfaces" are plotted rather than curves. In this study these relationships are calculated using THERMOCALC [16]. In this study the TCFE2 THERMOCALC database is used in order to capture the phases formed in stainless steel – titanium mixtures. Each material database includes polynomials which describe the Gibbs free energy of individual phases in a system as a function of temperature and composition and are developed with the aid of experimental information as well as Gibbs energy models [16]. By determining the phases with the lowest free energies at different temperature/composition values, multi-component phase diagrams can be calculated. In addition, the equilibrium phase evolution during solidification of a material can be determined as a function of temperature.

EXPERIMENTAL SETUP

Titanium Grade 2 (HCP α-phase) and Stainless Steel 316 (FCC γ-phase) coupons measuring 50mm x 36mm x 0.8mm were sectioned from rolled sheets. The surfaces of the samples were sanded with aluminum oxide abrasive pads with an equivalent grit of roughly 100 to remove impurities and dull any polished surfaces and cleaned with acetone immediately prior to welding. Welds were performed in a butt-weld geometry with the SS coupon

clamped in a fixture and the Ti coupon placed next to it with no gap. The lack of a gap between the plates and free movement of the Ti coupon limits the thermal stresses induced by the welding process [17]. The samples were welded using a pulsed Nd:YAG laser at a wavelength of 1064nm and a maximum average power of 2kW. The diameter of the Gaussian laser spot on the sample surface was 1mm. Laser pulses were produced at controlled repetition rate of 100Hz, each with a rectangular temporal pulse profile. A 6-axis robotic arm with an end effector was used for positioning and translation at a constant speed of 20mm/s to achieve constant pulse overlaps. Additionally, ultra-high-purity Argon gas was used to shield the weld pool from atmospheric contamination along the top and bottom surfaces of the weld. A schematic diagram of the process is shown in Fig. 2.

Processing parameters were chosen using a 3-level, 3-factor design of experiment array. The three factors analyzed were the laser beam offset from the SS-Ti interface, pulse duration, and average power. Samples were processed at offsets of 0, 150, and 300μm from the SS-Ti interface toward the Ti plate, pulse durations of ~2.5, 3.6, and 6.5ms, and average powers of 300, 525, and 750W. For a constant average power and repetition rate, changes in the pulse duration were accompanied by changes in the peak power in order to maintain constant pulse energy. Welded samples were sectioned using wire electrical discharge machining (EDM) into small samples for cross-section analysis as well as dog-bone samples for tensile testing. The dog-bone samples were cut to sub-size specimen specifications as defined in ASTM standard #E8-09 [18].

Samples for cross-sectional analysis were ground using carbide paper and then polished using alumina slurries. After polishing the titanium was etched using Kroll's reagent while the stainless steel was etched using a mixture of nitric acid, hydrofluoric acid, and water. Compositional analysis was performed using energy-dispersive x-ray spectroscopy (EDX) and crystal structure analysis was performed using electron backscatter diffraction (EBSD).

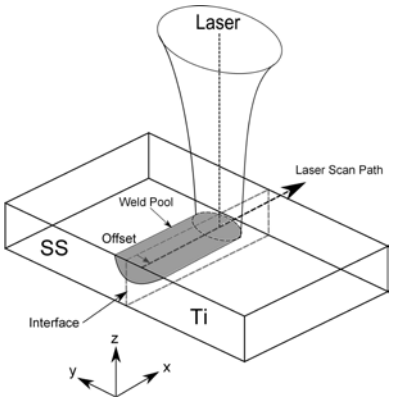

Figure 2. Schematic diagram of welding geometry. Note offset of laser beam from interface toward Ti sample.

Surface morphologies were observed using a scanning electron microscope (SEM) and tensile testing was performed using a uniaxial tensile testing machine operating at a cross-head speed of 0.1mm/min.

RESULTS AND DISCUSSION

Weld Geometry

Figure 3 is a typical weld cross-section (yz-plane) for samples processed at an average power of 750W. The weld pool is observed to be confined to the upper portion of the plates and some variation in symmetry about the original SS-Ti interface was observed for different laser offsets as expected due to the large differences in material properties across the weld interface. The thermal diffusivity for Ti, 6.9e-6 m^2/s, is almost twice that of SS, 4.08e-6 m^2/s, and Ti also has a higher melting temperature, 1665°C versus 1375°C. This requires a greater amount of heat to be supplied to the Ti in order to ensure it reaches its melting temperature which is achieved through the offset of the laser beam toward the Ti. Samples processed at high powers show greater penetration and weld size compared to lower powers. The weld cross-section, however, shows that full penetration is not achieved even for the highest power welds. The use of a smaller laser spot size and higher power would likely allow for full penetration welds to be performed for similar thickness plates.

The top weld surface as observed from the cross-section in Fig. 3 is flat and nearly flush with the base Ti and SS plates. The minimal gap between the plates and lack of filler material results in weld pools without any buildup above the surface of the original plates. This surface morphology is aided by the lack of full penetration into the welds. Currently the weld pool is supported by the underlying solid material. Full penetration may allow for gravitational effects to pull down the molten material resulting in concave weld surfaces.

Table 1. Failure stresses from tensile tests. Note large variance in strength. Samples with no stress value fractured upon solidification.

Con-dition	Offset (μm)	Pulse Duration (ms)	Failure Stress (MPa)
1	0	6.5	81.4±72.5
2	150	6.5	41.1±12.0
3	300	6.5	-
4	0	3.6	65.1±2.8
5	150	3.7	-
6	300	3.7	81.0±64.1
7	0	2.5	-
8	150	2.5	-
9	300	2.5	-

Weld Strength

Fracture stress values for samples processed at an average power of 750W with various offsets and pulse durations are shown in Table 1. Load-extension curves acquired during tensile testing showed no evidence of appreciable plastic deformation and no necking was observed suggesting primarily brittle fracture of the weld joints. Samples processed at the highest average power, 750W, were chosen for analysis in this study due to their greater penetration depth. All samples processed at this power fractured at the weld joint rather than in the base material and fracture occurred closer to the SS-side of the weld zone. Fracture stress values were calculated using the maximum load observed during tensile testing and the fracture surface area (xz-plane) observed under optical microscopy. The fracture stress values reported in Table 1 show that the weld joints are weaker than the base metal even when considering their smaller cross-sectional area and have a great deal of scatter between samples. The strongest samples were able to achieve a failure stress that was ~60% of the yield stress of Stainless Steel and ~35% of the ultimate tensile strength of Titanium. Ideally, the weld itself should be stronger than the base material and in the case of dissimilar material welds, should be stronger than the weaker of the two materials being joined. Thus these initial results suggest that further understanding of the microstructure and failure mechanisms in stainless steel to Titanium dissimilar material welds is required to form joints of adequate strength.

The lack of necking during tensile testing of the welds along with the large scatter in tensile strengths show high sensitivity to initial cracks within the weld and again suggests that brittle fracture is the main failure mode. Audible cracking was noted during cooling of the welds after solidification which varied in degree for different processing parameters. Samples processed at the shortest pulse duration of ~2.5ms and thus the highest peak power, are not included in Table 1 due to extensive cracking of the weld during cooling resulting in complete failure of the joints. Cracks similar to those shown in the cross-section in Fig. 11 were observed in the weld zone for a number of laser parameters and were typically oriented perpendicular to the laser scanning direction on the yz-plane and are likely caused by the difference in the coefficients of thermal expansion between the SS, ~16e-6 m/m/°C, and Ti, ~9e-6 m/m/°C. After the laser passes, assuming the two materials are initially at the same temperature, the stainless steel will undergo a greater degree of contraction than the titanium during cooling. Since the two materials are joined, this discrepancy leads to the formation of tensile stresses and cracks in the SS-side and compressive stresses in the Ti-side of the weld.

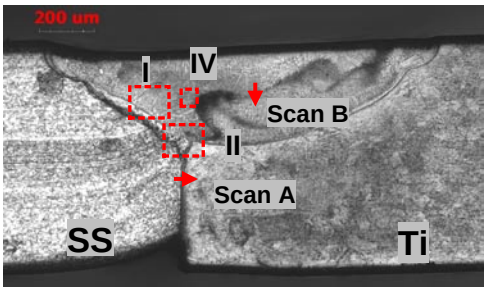

Figure 3. Typical weld cross-section (yz-plane). Note asymmetry of weld pool and existence of various microstructures within weld pool. Laser Power: 750W, Offset 300µm, Pulse Width: 3.7ms, Scan Speed: 20mm/s

Weld-Pool Microstructure and Composition

Several different microstructures are observed in the weld pool in Fig. 3. A distinct layer lines the SS-weld pool interface, passing through the lower left corner of region I, while further into the melt pool on the SS-side, a coarse dendrite-like morphology is observed which extends across the top of the weld pool toward the Ti-side. The majority of the Ti-side of the weld pool shows a finer microstructure. Some indication of joining below the weld zone is seen as well in region II of the image. Figure 4 shows higher magnification optical micrographs of two sections outlined in Fig. 3. Dendrites are clearly observed in Fig. 4a, along with a layer separating them from the base stainless steel. The existence of dendrites oriented primarily normal to the solid-liquid interface suggests directional solidification from the interface toward the center of the weld pool. Figure 4b shows the area below the main weld pool and a thin melt zone between the two sheets is observed. Since welds performed in this study are within the conduction welding mode, this joining below the main weld pool is considered to be caused by heat accumulation at the interface resulting in localized melting of the materials or weld pool flow along the interface.

Figure 5 shows an EDX line scan across Scan B as depicted in Fig. 3. While the average compositions across the coarse/fine microstructure boundary are nearly identical, the coarse dendrite structure shows significantly more variation in the composition. The average composition of ~70 at% Ti, ~20 at% Fe, and ~3 at% Cr in

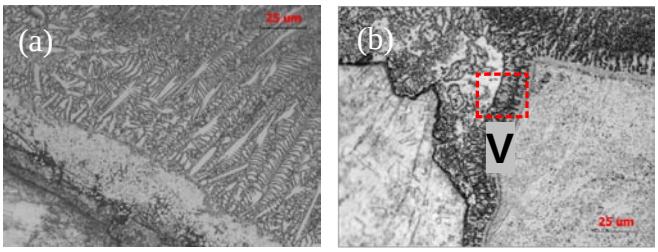

Figure 4. Optical micrographs of regions (a) I and (b) II from Fig. 3. Note coarse dendritic structure in region I and joining in the form of a thin molten layer in region II.

addition to small amounts of Ni, Mo, and Mn when considered in the context of the binary Fe-Ti phase diagram suggests formation of a β-Ti/FeTi eutectic.

Figure 6 shows the composition profile across dendrites in the coarse dendrite region toward the SS-side of the weld pool. Clear differentiation between the dendrite and interdendritic regions is observed in Fig. 6a with the Ti and Fe compositions moving in opposite directions. The average composition of the Ti-rich regions (interdendritic regions) is ~75 at% Ti and ~18 at% Fe with the remainder being taken up by components such as Mo and Cr. The dendritic regions have a more balanced composition with the Ti composition nearing ~50 at% and the Fe compositionnearing ~40 at%. While these two compositions are different from those expected during equilibrium eutectic solidification, it has been shown that rapid solidification will cause extended solubility in β-Ti and TiFe [14]. Thus, initial compositional analysis suggests that the dendrites are TiFe and the interdendritic regions are supersaturated β-Ti.

An EBSD surface map of a region containing a coarse dendritic microstructure (region IV in Fig. 3) is shown in Fig. 7. The euler angle map shown in Fig. 7b shows large regions with similar dendrite growth directions as having the same orientation. These areas include the darker interdendritic regions as well. Each of these regions with the same crystal orientation are considered to be eutectic colonies. Both the dendritic and interdendritic regions show a BCC structure which when considered in terms of the equilibrium phase diagrams suggests a β-Ti/FeTi mixture. The composition of these dendrites and their interdendrite regions were shown to be close to TiFe and β-Ti, respectively. Both of these phases have a BCC crystal structure. The observation of BCC structure through EBSD is further evidence that these structures are in fact TiFe dendrites in a supersaturated β-Ti matrix.

A line scan EDX profile across the lower portion of the weld interface (scan A in Fig. 3) is shown in Fig. 8 and

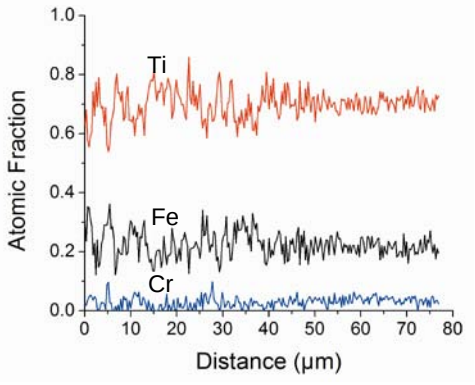

Figure 5. EDX line scan across SS-Ti interface (Scan B in Fig. 3). Note difference in composition uniformity across interface.

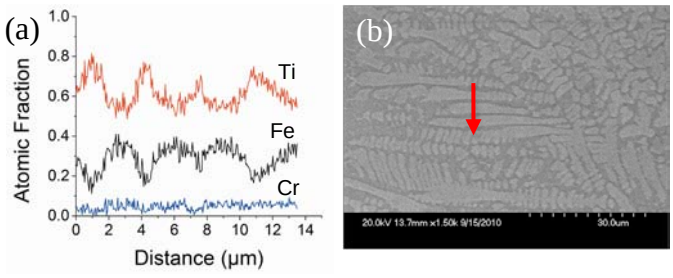

Figure 6. EDX line scan across coarse dendrites observed on cross-section (yz-plane). Note higher Ti content in interdendrite regions.

clearly shows the existence of a mixed layer at the interface with a composition between that of pure SS and pure Ti. The composition abruptly changes at the SS interface while the transition is more gradual on the Ti-side of the joint. This is likely due to the higher diffusivity of Fe and Cr into Ti than Ti into Fe and Cr [19]. The mixed zone is observed to also have a similar composition to that observed in the dendritic regions of the weld pool as discussed above. This again suggests a mixture of FeTi and β-Ti in this region, however, no significant fluctuations in composition are observed across the interface or along the interface in the z-direction (not shown). If FeTi regions were to exist in this region a similar profile to that observed in Fig. 6 would be expected. As discussed above, extended solubility of Fe in the β-Ti structure has been shown to occur for high cooling rates such as those experienced during laser welding [14], however, within the main weld pool dendrites of TiFe were seen to form. Thus, the cooling rate in the lower section of the weld must be significantly higher such that a single-phase region is formed from a eutectic composition. This high cooling rate is likely due to the thin film-like geometry of the molten zone with a thickness of roughly 4μm. The large surface area connecting the molten material to the surrounding solid on both sides of the interface and the limited volume of molten material would allow for a

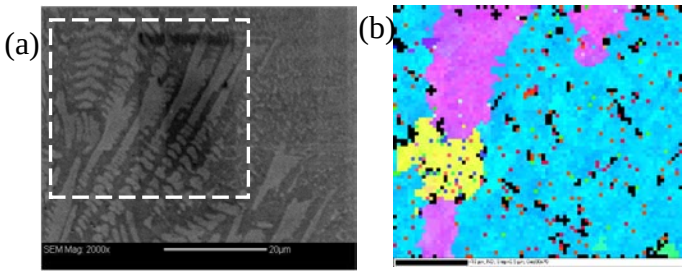

Figure 7. EBSD scan of area IV in Fig. 3. (a) SEM scan showing dendritic structure and EBSD measured area (outlined). (b) Euler angle map of measured area from (a) showing various crystal orientations within eutectic colonies.

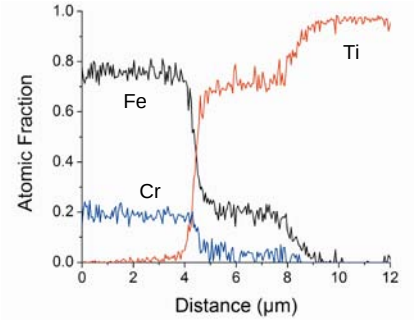

Figure 8. EDX line scan across SS-Ti interface (Scan A in Fig. 3). Note homogeneous composition within weld zone and significant diffusion of Fe and Cr into Ti.

significant increase in the cooling rate within this region.

Figure 9 shows EBSD scans of an area where a layered structure is observed in the weld pool (region V in Fig. 4b). The lighter colored region on the left of Fig. 9a was determined by EDX to be a nearly equiatomic Ti-Fe layer and the darker colored region a ~70 at% Ti layer that extends from the bottom of the main melt pool toward the bottom of the joint. Fig. 9b is a structure map of the same region with BCC structured regions colored red and hexagonal close-packed (HCP) structured regions colored green. The layer closer to the SS-side of the weld exhibits a HCP structure while the layer closer to the Ti-side of the weld shows a BCC structure. The BCC structure, along with the homogeneous composition of roughly 70 at% Ti and 20 at% Fe suggests that this layer is comprised of β-Ti grains supersaturated with Fe. As discussed above, the adjacent HCP layer has a composition which, at equilibrium, would form a mixture of FeTi and $TiFe_2$ (λ-Laves). The observation of a hexagonal structure through EBSD suggests that this layer consists primarily of $TiFe_2$.

Phase development curves for materials with similar compositions to those observed in the aforementioned layers modeled using CALPHAD techniques are shown in Fig. 10a and 10b. Figure 10a shows the mole fraction of phases present in a material with a composition of 18.19% Fe, 74.00% Ti, 4.53% Cr, 1.38% Ni, 1.66% Mn, and 0.23 at% Mo, as a function of temperature. This composition is

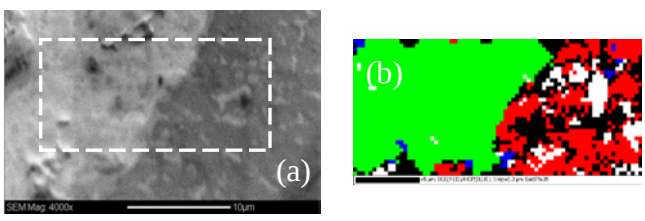

Figure 9. EBSD scan of area V in Fig. 4(b). (a) SEM scan showing layered structure as well as EBSD measured area (outlined). (b) Structure map of measured area with red indicating BCC and green indicating HCP structures.

very similar to that observed in the Ti-rich interfacial layer as well as in the main weld pool as determined through EDX. The model suggests that the first phase to form at roughly 1250°C is BCC or β-Ti. Once the temperature has reached ~900°C the intermetallic phase, FeTi, starts to form. In the main weld pool a microstructure consisting of TiFe dendrites within a β-Ti matrix was observed. This phase mixture is consistent with that predicted by the CALPHAD model at this composition. The Ti-rich interfacial layer showed a BCC structure and a homogeneous Ti-rich composition. The lack of TiFe in this layer is considered to be due to the high quench rate experienced by the thin interfacial layer during solidification. As the model shows, even at equilibrium, the β-Ti begins to form at a temperature over 300°C above the FeTi. At high quench rates it has been shown that TiFe may not have time to nucleate and grow resulting in a single-phase region near the eutectic composition [15].

Figure 10b shows the mole fraction of phases present

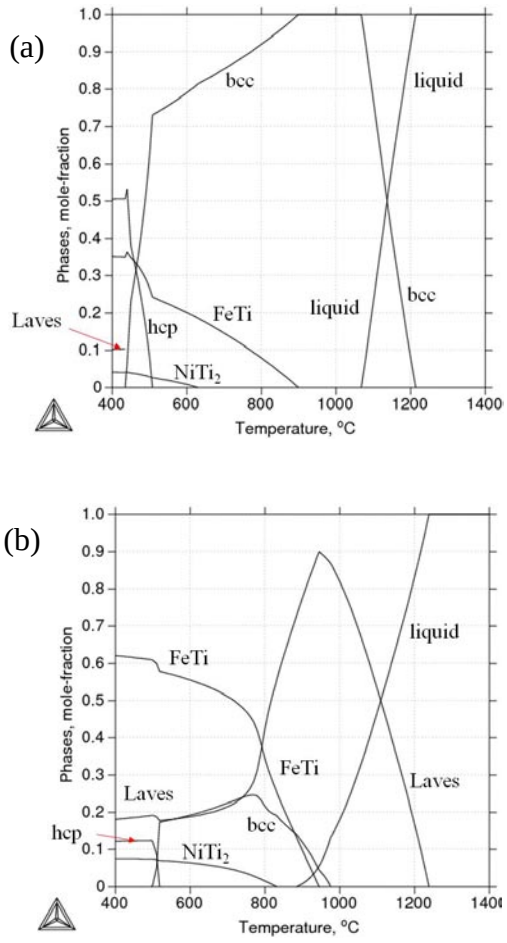

Figure 10. Simulation results for mole fraction of phases for (a) 18.19% Fe, 74.00% Ti, 4.53% Cr, 1.38% Ni, 1.66% Mn, 0.23 at% Mo and (b) 37.00% Fe, 46.59% Ti, 10.70% Cr, 2.95 % Ni, 2.47% Mn, 0.29 at% Mo regions.

in a material with a composition of 37.00% Fe, 46.59% Ti, 10.70% Cr, 2.95% Ni, 2.47% Mn, and 0.29 at% Mo as a function of temperature. This composition is very similar to that observed in the near-equiatomic layer toward the SS-side of the joint in Fig. 4b. The model predicts the initial formation of the Laves phase, $TiFe_2$, with FeTi forming at a temperature a few hundred degrees lower. Thus the existence of predominantly $TiFe_2$ in the near-equiatomic interfacial layer is consistent with the CALPHAD model and is likely due to the high quench rate in the lower weld zone. The material in this section does not have sufficient time for TiFe formation during solidification.

Fracture Surface Analysis

Fracture surfaces created during tensile testing of the welded samples were analyzed using SEM and EDX in order to determine the fracture mode and position of the crack within the weld pool. As noted above, low-magnification observation of the fracture surfaces showed that fracture always occurred along the original SS-Ti interface position or toward the SS-side of the weld pool. Figure 11 is an SEM image of a typical SS fracture surface (xz-plane). The brighter region toward the top of the image is the top surface of the weld (xy-plane). Cracks can be observed propagating in the yz-plane on the upper part of the weld joint and can be seen on the top surface of the weld as well. The lighter colored region with the long horizontal lines at the bottom of the image is the unwelded portion of the plate. The fracture surface shown in Fig. 11 depicts significantly different fracture surfaces along the top and bottom halves of weld. The surface of the bottom half is punctuated by equally spaced lines oriented perpendicular to the laser scan direction. In contrast, the upper fracture surface consists of larger contiguous areas with more significant topographical changes.

Figure 12a shows a higher magnification SEM image of region VIII in the upper fracture surface. A large smooth region on the order of a few hundred micrometers tall is observed on the left of the image with a number of finger-like features observed on the right. The composition of this region as determined through EDX was ~70 at% Ti and ~20 at% Fe and was observed to be homogenous throughout. This overall composition is very close to that observed in the interdendritic regions of the main weld pool as shown in Fig. 6. EDX analysis of the corresponding Ti fracture surface showed a nearly identical composition. This suggests that fracture occurred within the interdendritic regions in the main weld pool rather than at the dendrite surfaces. As observed in Fig. 11, however, the entire upper fracture surface does not have this same smooth surface morphology. Figure 12b is a high-magnification SEM image of region IX in Fig. 11. The surface roughness is observed to be greater than region VIII and the composition is found to be much closer to the roughly 50 at% Ti and 35 at% Fe observed in the Laves-phase layer toward the SS-side of the weld zone in Fig. 3. Regions with this rough fracture surface and low Ti-content are found to consistently occur closer to the SS-side of the weld pool than the smooth Ti-rich regions.

Fracture in the main weld zone of the material is thus observed to occur within two different regions of the weld pool, the first being the interdendritic zones in the coarse dendritic microstructure located toward the SS-side of the weld pool and the second being the layer of Laves phase lining the SS-weld pool interface. It is important to note that fracture surfaces originating in the coarse dendritic microstructure regions almost exclusively showed a smooth surface structure at high magnification and were always nearly perpendicular to the applied tensile load direction. This surface morphology and crack geometry suggests that all of these regions failed through interdendritic cracking between dendrites that were oriented nearly perpendicular to the loading direction. Fracture also occurs in the Laves phase layer on the SS-weld pool interface which is oriented at an angle with respect to the applied tensile load. It is considered that in regions where fracture is observed in the Laves phase, the TiFe dendrites are primarily oriented parallel to the tensile loading direction resulting in greater strength.

A high magnification SEM image of the lower fracture surface from Fig. 11 is shown in Fig. 13. The surface appears rougher than that observed in the interdendritic fracture surfaces in the main weld pool suggesting a different fracture mechanism is active in this region. Figure 14a is an EDX line scan performed across

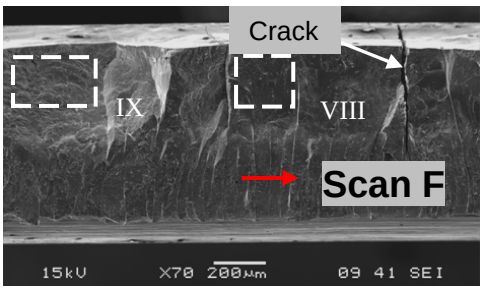

Figure 11. Fracture surface (SS-side, typical). Note different morphologies in upper and lower sections.

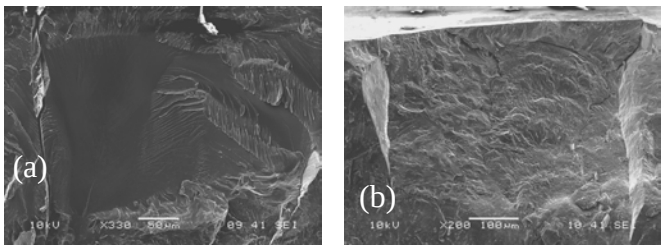

Figure 12. SEM images of regions (a) VIII and (b) IX from Fig. 11. Note large, smooth fracture surface in region VIII and rough surface in region IX.

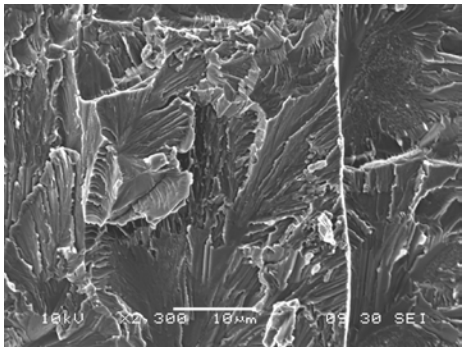

Figure 13. SEM image of lower fracture surface in Fig. 11. Note vertically oriented cracks formed through grains and surface indicative of cleavage fracture.

the lower interface in the x-direction (scan F in Fig. 11). The composition is seen to fluctuate significantly within this scan and small sections with the same composition are observed. Upon careful analysis it is found that the composition changes at each vertical line between Ti-rich and Fe-rich suggesting that either different phases are formed alternately along the x-direction or that there are height differences between the different sections.

Figure 14b is a topographical line profile obtained along scan F in Fig. 11 through optical profilometry. The profile shows significant topographic variation along the laser scan direction with a period very similar to that observed in the composition profile in Fig. 14a. The vertical lines observed in the SEM images are considered to be cracks in the yz-plane which separate regions located closer to the SS and Ti-sides of the thin melt zone. This structure can be understood in the context of Fig. 8, the compositional profile across the lower weld pool interface. As discussed previously, the composition within the lower weld pool is homogeneous. The two main compositions observed on the lower fracture surface (Fig. 14a) are ~70 at% Ti/20 at% Fe and ~20 at%Ti/60 at% Fe. In Fig. 8, these two compositions occur at different locations. The ~70 at%

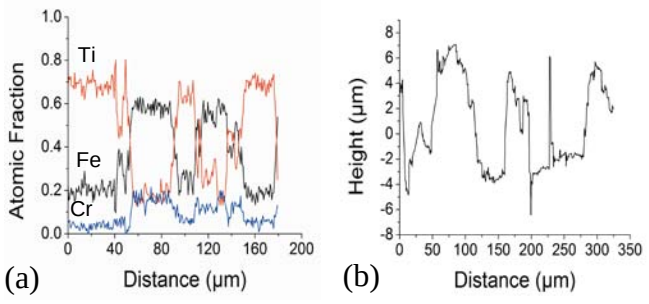

Figure 14. (a) EDX composition profile and (b) topographic profile across lower fracture surface (scan F in Fig. 11). Abrupt changes in composition and height coincide with the periodic vertical crack-like features.

Ti composition occurs across the entire weld pool while the ~60 at% Fe composition only occurs at the interface between the base SS and the weld pool. When considered in the context of Fig. 14b which shows a height difference between adjacent surfaces of roughly 8μm which is on the order of the width of the lower weld pool, it is likely that fracture is occurring alternately on the SS-weld and Ti-weld interfaces. Movement of the crack between the SS-weld and Ti-weld interfaces may be due to cracks formed by thermal stresses during cooling of the dissimilar weld joint.

Further Discussion

While brittle fracture was observed within the weld, the different microstructures and phases formed within and below the main weld pool show different fracture morphologies. In the lower weld zone, the existence of a supersaturated single-phase rather than a eutectic microstructure seems to cause failure to occur in an intragranular manner along the SS-weld and Ti-weld interfaces resulting in significant fracture surface area. Transitions between fracture along the SS and Ti sides of the joint are believed to occur along cracks formed perpendicular to the laser scan path during solidification and cooling of the joints. The dendritic regions in the main weld pool have an average composition nearly identical to that in the lower weld zone; however, due to their microstructure the fracture surfaces are significantly larger and smoother. The lower weld zone structure likely requires more energy for crack propagation than the dendritic structures observed in the upper weld zone which are particularly weak transverse to the direction of dendrite growth. The formation of the isotropic single-phase structure below the main weld pool is likely due to the high quench rate experienced by the thin molten layer. This indicates that a uniform, high quench rate throughout the entire weld pool may be beneficial to the strength of SS-Ti dissimilar material welds due to the elimination of the anisotropic dendritic structures. This requires careful control over the weld geometry and favors a weld pool with minimal volume and uniform thickness. A new joining process being developed by the authors aims to achieve such a joint geometry by utilizing thermal accumulation at the joint interface to form a thin layer of molten material. A shaped laser beam is scanned toward the joint to produce a weld pool that can be smaller than the beam diameter and produce a braze-like joint between dissimilar materials without the use of filler materials. Details on the proposed process will be the topic of a future study.

CONCLUSION

Laser fusion welded dissimilar joints between stainless steel 316 and titanium grade 2 have been investigated as a simplified model for the NiTi - stainless steel dissimilar material pair. Tensile strengths of the joints are observed to

be lower than the base materials with failure occurring through brittle fracture. EDX and EBSD analysis indicated the formation of coarse intermetallic TiFe dendrites within a β-Ti matrix in the main weld pool and single-phase supersaturated β-Ti(Fe) in the lower weld zone. Fracture surface analysis suggests that smooth interdendritic fracture between dendrites oriented perpendicular to the tensile load is the predominant mechanism of failure in the main weld pool while alternating failure along the SS-weld and Ti-weld interfaces was observed in the lower weld zone. Significantly greater surface area formation was observed in the lower portion of the weld suggesting that the single-phase supersaturated β-Ti(Fe) structure may be beneficial for fracture resistance. The specific fracture morphologies observed and preferential cracking within the coarse dendritic microstructure observed near the stainless-steel base material in the main weld pool suggests that control over the weld pool geometry, heat flow, and quench rate may allow for robust dissimilar metal welds between titanium and stainless steel.

ACKNOWLEDGEMENT

The authors would like to acknowledge Prof. James S. Im of the Materials Science Program in the Department of Applied Physics and Applied Mathematics and the Materials Research Science and Engineering Center, Columbia University for the use of their equipment.

REFERENCES

[1] Bauer I, Russek UA, Herfurth HJ, Witte R, Heinemann S, Newaz G, Mian A, Georgiev D, and Auner GW (2004) Laser microjoining of dissimilar and biocompatible materials. *Proceedings of SPIE*, pp. 454-464.

[2] Ghosh M, and Chatterjee S (2005) Effect of interface microstructure on the bond strength of the diffusion welded joints between titanium and stainless steel, *Materials Characterization* **54**(4-5), pp. 327-337.

[3] Lee MK, Lee JG, Choi YH, Kim DW, Rhee CK, Lee YB, and Hong SJ (2010) Interlayer engineering for dissimilar bonding of titanium to stainless steel, *Materials Letters* **64**(9), pp. 1105-1108.

[4] Li M, Sun D, Qiu X, Liu J, Miao K, and Wu W (2007) Effects of silver based filler metals on microstructure and properties of laser brazed joints between TiNi shape memory alloy and stainless steel, *Science And Technology of Welding and Joining* **12**(2), pp. 183-189.

[5] Ghosh M, and Chatterjee S (2002) Characterization of transition joints of commercially pure titanium to 304 stainless steel, *Materials Characterization* **48**(5), pp. 393-399.

[6] Raghavan V (1987) *Phase Diagrams of Ternay Iron Alloys*, ASM International, Metals Park, OH.

[7] Sun Z, and Ion JC (1995) Review Laser welding of dissimilar metal combinations, *Journal of Materials Science* **30**, pp. 4205-4214.

[8] Vollertsen F, and Grupp M (2005) Laser beam joining of dissimilar thin sheet materials, *Steel Research International* **76**(2), pp. 240-244.

[9] Li MG, Sun DQ, Qiu XM, and Yin SQ (2006) Corrosion behavior of the laser-brazed joint of TiNi shape memory alloy and stainless steel in artificial saliva, *Materials Science and Engineering A* **441**, pp. 271-277.

[10] Kundu S, Ghosh M, Laik A, Bhanumurthy K, Kale G, and Chatterjee S (2005) Diffusion bonding of commercially pure titanium to 304 stainless steel using copper interlayer, *Materials Science and Engineering: A* **407**(1-2), pp. 154-160.

[11] Graff K (2005) *New Developments in Advanced Welding*, Woodhead Publishing, Cambridge.

[12] Yu C, Wu MF, and Lu H (2006) Factors influencing formation and growth of coarse Ti – Fe compound in Ti – Fe eutectic reaction, *Science And Technology* **11**(3), pp. 265-271.

[13] Louzguine-Luzgin, Dmitri V, Louzguina-Luzgina, Larissa V, Kato, Hidemi, Inoue A (2005) Non-equilibrium Ti-Fe bulk alloys with ultra-high strength and enhanced ductility, *Materials Research Society Symposium Proceedings* **851**, pp. 3-8.

[14] Polmear I (2005) *Light Alloys*, Butterworth-Heinemann.

[15] Ray R (1972) The constitution of metastable titanium-rich Ti-Fe alloys:An order-disorder transition, *Metallurgical Transactions* **126**(3), pp. 362-629.

[16] Gordon P (1983) *Principles of phase diagrams in materials systems*, Robert E. Krieger Publishing Company, Malabar, Fla.

[17] Jansson B (1993) The Thermo Calc project, *Thermochimica Acta* **214**(1), pp. 93-96.

[18] Ely KJ (2001) Conduction Welding, *Handbook of Laser Materials Processing*, Magnolia Publishing, Orlando, Fl, pp. 354-357.

[19] ASTM (2009) *Standard Test Methods for Tension Testing of Metallic Materials*, ASTM International, West Conshohocken, PA.

[20] Kale GB, Patil RV, and Gawade PS (1998) Interdiffusion studies in titanium-304 stainless steel system, *Journal of Nuclear Materials* **257**(May), pp. 44-50.